ARTICLE

Two-Dimensional Polymer Synthesized *via* Solid-State Polymerization for High-Performance Supercapacitors

Wei Liu,[†,‡,§,#] Mani Ulaganathan,[∥,⊥,#] Ibrahim Abdelwahab,[†,§] Xin Luo,[‡,¶] Zhongxin Chen,[†,§] Sherman Jun Rong Tan,[†,§] Xiaowei Wang,[†,§] Yanpeng Liu,[†] Dechao Geng,[†] Yang Bao,[†] Jianyi Chen,[†] and Kian Ping Loh*,[†,‡]
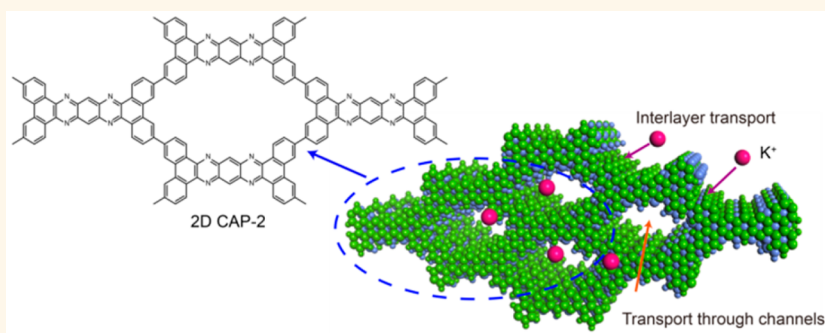
[†]Department of Chemistry, National University of Singapore, 3 Science Drive 3, 117543 Singapore
[‡]Centre for Advanced 2-D Materials (CA2DM), National University of Singapore, 6 Science Drive 2, 117546 Singapore
[§]NUS Graduate School for Integrative Sciences and Engineering, National University of Singapore, Centre for Life Sciences, #05-01, 28 Medical Drive, 117456 Singapore
[∥]School of Materials Science and Engineering, Nanyang Technological University, 639798 Singapore

ⓢ *Supporting Information*

ABSTRACT: Two-dimensional (2-D) polymer has properties that are attractive for energy storage applications because of its combination of heteroatoms, porosities and layered structure, which provides redox chemistry and ion diffusion routes through the 2-D planes and 1-D channels. Here, conjugated aromatic polymers (CAPs) were synthesized in quantitative yield *via* solid-state polymerization of phenazine-based precursor crystals. By choosing flat molecules (2-TBTBP and 3-TBQP) with different positions of bromine substituents on a phenazine-derived scaffold, C−C cross coupling was induced following thermal debromination. CAP-2 is polymerized from monomers that have been prepacked into layered structure (3-TBQP). It can be mechanically exfoliated into micrometer-sized ultrathin sheets that show sharp Raman peaks which reflect conformational ordering. CAP-2 has a dominant pore size of ∼0.8 nm; when applied as an asymmetric supercapacitor, it delivers a specific capacitance of 233 F g^{-1} at a current density of 1.0 A g^{-1}, and shows outstanding cycle performance.

KEYWORDS: *solid-state polymerization, C−C coupling, 2-D materials, conjugated porous polymers, supercapacitors*

Electrochemical capacitors or supercapacitors have drawn great attention owing to their high power capability and excellent cycle performance.[1] However, conventional activated carbon-based electrodes have relatively low energy density (less than 6 Wh kg^{-1} for commercial supercapacitors).[2] To address this, there are intense research efforts for the design of new carbonaceous materials with improved specific surface area, highly homogeneous pore size distribution and heteroatoms into the carbonaceous electrodes.[3] Bottom-up synthesis of conjugated porous frameworks allows the construction of semiconducting organic networks with tunable pore size and properties, which offers great opportunities for developing green organic electrodes for applications in energy storage.[4−7] However, conjugated porous frameworks synthesized *via* wet chemistry methods suffer from insufficient electrical conductivity.[8] Moreover, wet chemistry methods employing noble metal catalysts to produce porous polymers are challenging to scale up.
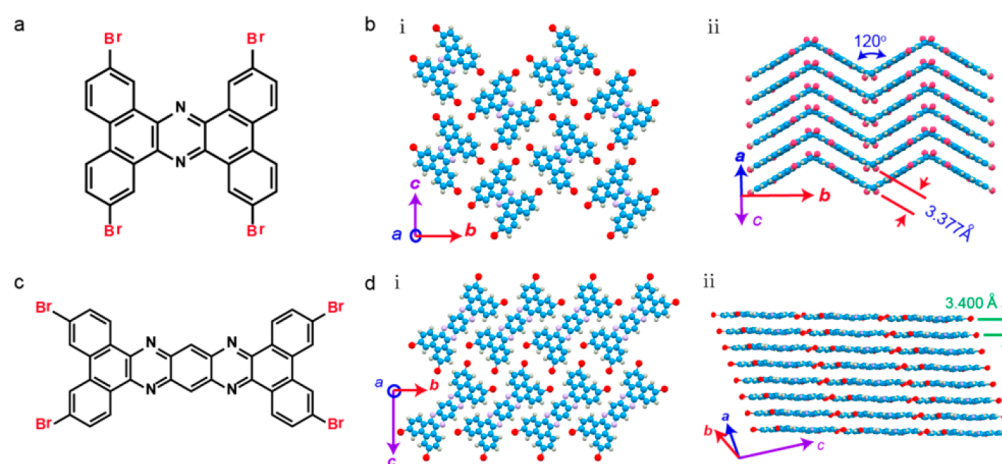
Figure 1. Crystallographic data of monomers. (a) Chemical structure of 2-TBTBP. (b) Crystallographic packing of 2-TBTBP shown as ball−stick model (i, top-view, ii, side-view). (c) Chemical structure of 3-TBQP. (d) Crystallographic packing of 3-TBQP shown as ball−stick model (i, top-view, ii, side-view).

2-D polymer has properties that are attractive for energy storage applications because of its combination of porosities and layered structure, which provides ion diffusion routes through the 2-D planes and 1-D channels. In addition, if the polymer has an aromatic conjugated scaffold, it mediates charge transfer. The key challenge of 2-D polymer synthesis is how to confine chain evolution in two dimensions. So far, thermodynamic approach has been used for producing 2-D covalent organic frameworks (2-D COFs) under reversible bond formation conditions, which allows for self-correction of energetically unfavorable products to achieve crystalline packing order.[7,9] Highly crystalline 2-D polymers have also been achieved by utilizing reversible self-addition polymerization between monomers prearranged into layered single crystals. The obtained 2-D polymer can be exfoliated into single layer crystals.[10−12] It is understood that dynamic covalent bonds formation using B−O, C−N type linkages *etc.* during crystal growth allows better quality crystallinity. However, this approach is disadvantaged by the poor chemical and thermal stability of the polymeric product. For example, the synthesized 2-D polymer single crystals made *via* cycloaddition reaction between preorganized molecules decomposed fully to its monomers upon slight heating.[11] Thus, it is desirable to produce 2-D conjugated polymers based on C−C coupling reactions which have stronger chemical bonds. However, it is difficult to confine C−C coupling reactions in two dimensions in an isotropic reaction medium without the help of a template.[13] For example, porous polymers synthesized *via* Suzuki coupling, Ullmann coupling and Yamamoto coupling are normally obtained in the form of fine powders.[14,15] In addition, wet chemistry methods employing noble metal catalysts usually produce conjugated porous polymers in milligram-scale, limiting their further applications in fields like energy storage or catalysis.

Recently, we reported a C−C coupling based 2-D conjugated polymer *via* endogenous polymerization of phenazine-based monomer carried out under catalyst- and solvent-free condition.[16] In this contribution, we extend the endogenous polymerization strategy to different phenazine-based monomers 2-TBTBP and 3-TBQP (Figure 1) that prepack into single crystals with different topologies. These are converted by endogenous polymerization into π-conjugated, nanoporous aromatic polymers (CAPs). Monomers 3-TBQP are densely packed into a quasi-2-D structure (Figure 1d), which is useful in confining C−C coupling reaction in two dimensions during the endogenous solid-state polymerization. The synthesized 2-D polymer shows distinct lamellar structure with highly regular pore size in the range of 0.7−1.0 nm, which is advantageous for supercapacitive energy storage. When employed as positive electrode in an asymmetric supercapacitor, it delivers a specific capacitance of 233 F g^{-1} at a current density of 1.0 A g^{-1} in 2 M KCl aqueous electrolyte. It shows an excellent cycle life with ∼80% capacity retention over 10 000 cycles. These results demonstrate that endogenous polymerization is a facile approach for preparing 2-D polymer with well-defined pores and conjugated aromatic structure, which can be used as green organic electrodes in supercapacitor applications.

RESULTS AND DISCUSSION

The monomers 2,7,11,16-tetrabromotetrabenzo[a,c,h,j]-phenazine (2-TBTBP) and 3,6,14,17-tetrabromodibenzo[a,c]-dibenzo[5,6:7,8]-quinoxalino-[2,3-i]phenazine (3-TBQP) (Figure 1) were prepared through condensation reactions between diamine and diketone derivatives in quantitative yield. The as-prepared 2-TBTBP and 3-TBQP crude products were sublimated in a three-heating-zone tube furnace to obtain single crystals (Synthesis and sublimation details are provided in methods). X-ray crystallographic analysis reveal that 2-TBTBP crystallizes in a centrosymmetric monoclinic space group $P2(1)/n$, with lattice parameters of a = 3.9742 (2) Å, b = 19.4868(11) Å, c = 14.9127(7) Å, β = 92.426(3)°, volume = 1153.87 Å^3. The typical layered structure of 2-TBTBP consisting of zigzag and parallel-stacked structure held by π−π interactions, multiple hydrogen bonding and van der Waals force is given in Figure 1b. Adjacent 2-TBTBP molecules which are nonparallel are stacked at a dihedral angle of ∼120° and interact with each other through hydrogen bonding. Adjacent parallel 2-TBTBP molecules are tightly packed through a displaced face-to-face π−π interaction and the distance between the aromatic planes is 3.38 Å. On the other hand, 3-TBQP crystallizes in a triclinic space group $P\bar{1}$, with lattice parameters of a = 3.8581 (2) Å, b = 10.5438(6) Å, c = 16.1258(9) Å, α = 96.687(3)° β = 96.766(2)°, γ = 95.701(2)°, volume = 642.717 Å^3. 3-TBQP molecules are packed into a 2-D lamellar network held by multiple hydrogen bonding and van der Waals force, as shown in Figure 1d. The adjacent coplanar
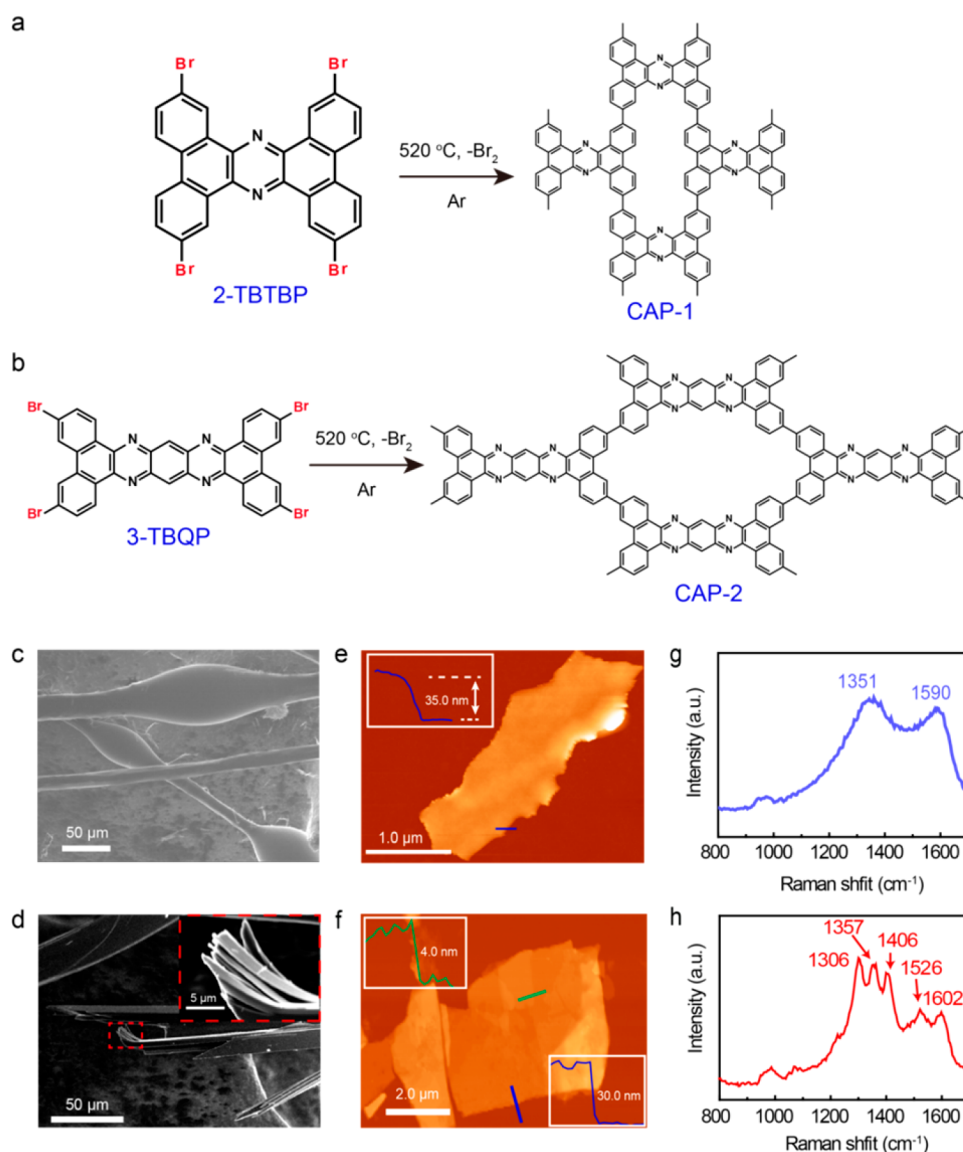
Figure 2. Synthesis and microscopy characterization of CAPs. (a,b) Synthesis of CAP-1 and CAP-2 *via* thermally initiated endogenous polymerization. (c,d) SEM images of CAP-1 (c) and CAP-2 (d). Insert: Enlarged image of the red dashed square area in (d), where the slightly twisted part reveals a clear lamellar structure. (e,f) AFM topography of exfoliated CAP-1 sheet (e) and CAP-2 sheet (f) on silicon wafer. Insert: Corresponding AFM height profiles of cross sections. (g,h) Raman spectra of exfoliated CAP-1 sheet (g) and CAP-2 sheet (h).

3-TBQP molecules interact *via* hydrogen bond between the H and Br atoms, and also H and N atoms. Besides the coplanar interactions, the adjacent parallel 3-TBQP molecules are tightly packed through a displaced face-to-face $\pi-\pi$ interaction and the distance between the aromatic planes is 3.40 Å.

The thermal stability of precursor molecules was studied by thermal gravimetric analysis (TGA) with a heating rate of 10 °C min^{-1} under nitrogen atmosphere in the range of 150 to 900 °C. The thermal decomposition of 3-TBQP starts at 520 °C (Figure S1). This weight loss stage is contributed by debromination which accounts for around 40% of the whole weight, in agreement with the theoretical value (39.76%). Owing to its relatively smaller molecular weight, the evaporation of 2-TBTBP starts at around 450 °C. To perform thermal polymerization, the precursor samples were placed in a quartz tube which is closed at one end, and heated in a tube furnace at 520 °C for 3 h. Except for a small amount of the precursor deposited at the low-temperature area of the tube

furnace, the weight of the residue following polymerization of 2-TBTBP and 3-TBQP are ∼48% and ∼61% (theoretical value: 51.68% and 59.95%), respectively. The weight losses are mainly contributed by debromination, which produce radicals-containing units for C−C cross-coupling. The products of polymerizing 2-TBTBP and 3-TBQP are denoted as CAP-1 and CAP-2, respectively. The X-ray photoelectron spectroscopy (XPS) spectra of monomers before and after polymerization are shown in Figure S3 and S4. Before polymerization, there are two characteristic peaks corresponding to Br $3p_{3/2}$ and Br $3p_{1/2}$ in both monomers, while the XPS spectra of CAP-1 and CAP-2 show an absence of element signal corresponding to Br atoms, indicating successful debromination. Elemental analysis (Table S1 and S2) and Fourier transform infrared spectroscopy (FTIR) (Figure S5) provide further evidence of debromination and concomitant polymerization.

After polymerization, the derivatives CAP-1 and CAP-2 are shown in Figure 2c and 2d. It can be seen that CAP-1 has a
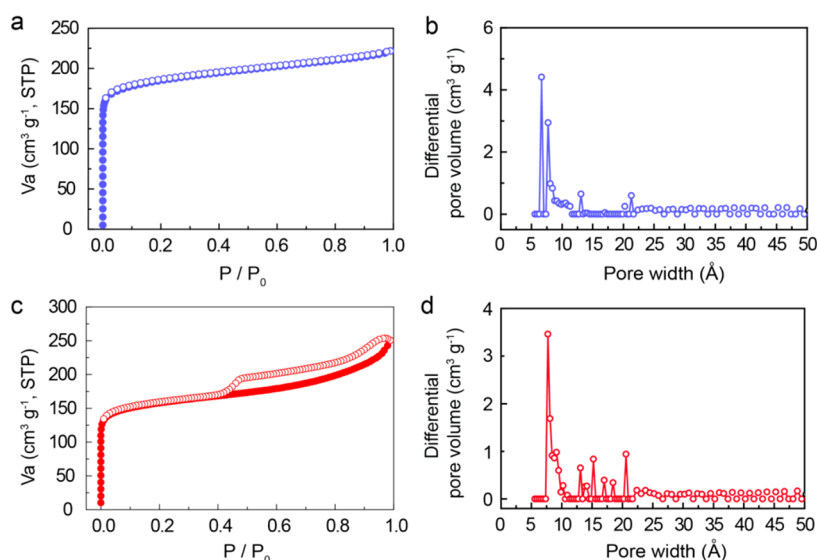
Figure 3. Nitrogen-gas sorption isotherm profiles CAPs. (a,c) Nitrogen adsorption (filled) and desorption (open) isotherm profiles of CAP-1 (a) and CAP-2 (c) at 77 K. (b,d) Pore size distribution of CAP-1 (b) and CAP-2 (d) calculated by nonlocal density functional theory (NLDFT) modeling based on N_2 adsorption data.
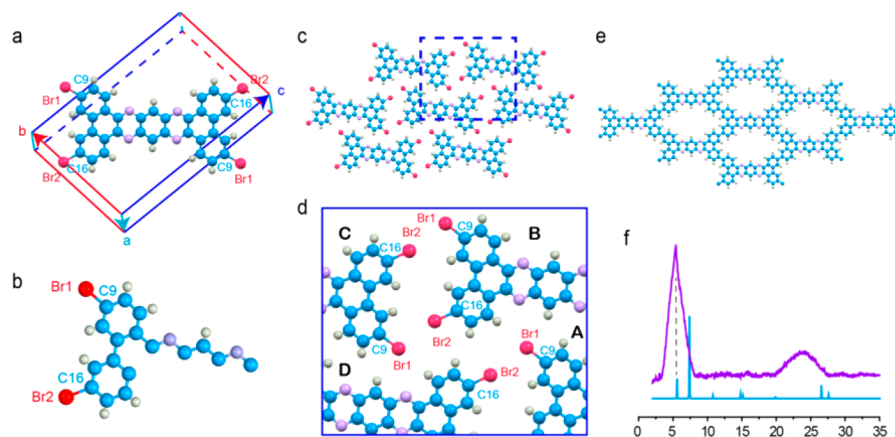

Figure 4. Reaction mechanism analysis. (a) Unit cell of 3-TBQP single crystal containing only one monomer. (b) 3-TBQP monomers in the same layer. (c) Enlarged image of the blue dashed square area in (b). (d) Structure of ideal CAP-2. (e) Monolayer of ideal CAP-2. (f) XRD profile obtained on CAP-2 (purple), and simulated XRD pattern using eclipsed stacking mode (blue).

beaded-fiber shape (Figure 2c), indicating that 2-TBTBP crystals partially melt during polymerization. On the other hand, CAP-2 retains the original needle shape of 3-TBQP with no sign of melting, which is a sign of solid-state polymerization (Figure 2d). The lamellar feature of CAP-2 can be easily observed under microscope (Figure 2d and insert). CAPs are mechanically exfoliated using scotch tape in a similar fashion to graphene and the exfoliated flakes are transferred onto silicon for AFM topographical analysis. The lateral size of the exfoliated sheets are in micrometer-scale. Figure 2e shows a CAP-1 sheet with a thickness ~35 nm. CAP-1 sheets show no clear lamellar structure. In contrast, the lamellar feature of CAP-2 can be easily observed under AFM. A CAP-2 sheet of ~6 μm with neat edge is observed (Figure 2f) and the AFM height profiles revealed that the sheet composed of layers ~4 nm in thickness. Full exfoliation of individual monolayer of CAP-2 is difficult due to the attractive Coulombic interlayer interactions and defects derived from interlayer covalent bonding. Although the 3-TBQP monomers are arranged in a quasi-2-D crystalline structure, polymerization requires consid-

erable movements of monomer units, during which, a small part of interlayer covalent bonding occurs inevitability.

Raman spectroscopy is a powerful technique for characterizing chain conformation and crystallinity in semicrystalline polymers. Figure 2g shows the Raman spectra of exfoliated CAP-1 sheet. CAP-1 shows two broad peaks at 1351 to 1590 cm^{-1}, similar to that of amorphous polymeric framework consisting of benzene rings and triazine rings.[17] This is consistent with the fact that no XRD peaks can be detected for CAP-1. During polymerization, the 2-TBTBP crystal is in a partially melted state, which causes random chain evolution and a randomly connected 3-D network in CAP-1. Its porous structure was investigated by N_2 sorption measurements at 77 K (Figure 3a and 3b), which shows a typical type I sorption profile for microabsorbents. The Brunauer−Emmett−Teller (BET) surface area and pore volume of CAP-1 derived from N_2 adsorption/desorption isotherm measurements are SA_{BET} = 704 m^2 g^{-1} and 0.34 cm^3 g^{-1}, respectively. In contrast, the Raman spectrum of CAP-2 (Figure 2h) shows 5 sharp peaks at 1306, 1357, 1406, 1526, 1602 cm^{-1}. Besides the vibrational
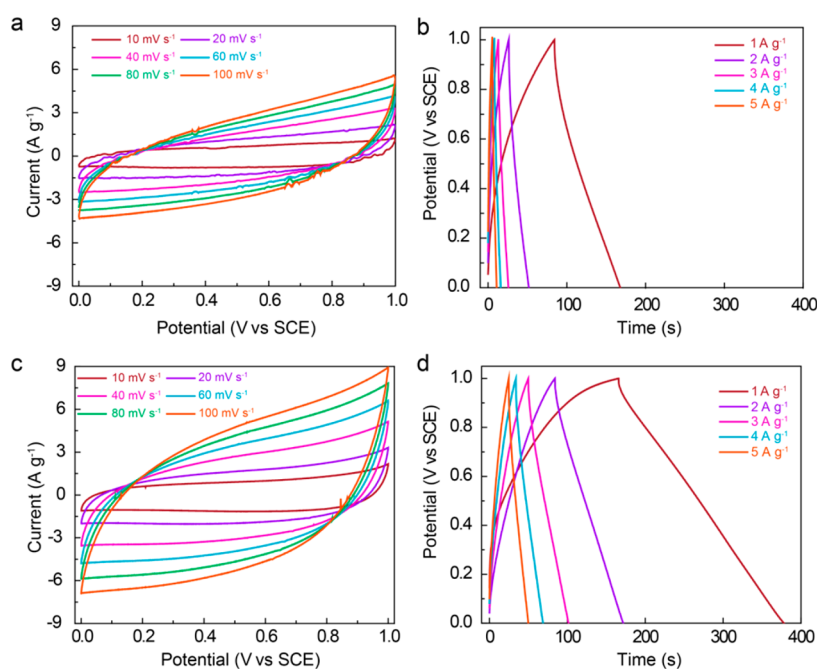
Figure 5. Electrochemical performance of CAP-s in a three-electrode setup. (a) Cyclic voltamograms of CAP-1 at different scan rates in 2 M KCl. (b) Galvanostatic charge/discharge profiles of CAP-1 at different current densities in 2 M KCl. (c) Cyclic voltamograms of CAP-2 at different scan rates in 2 M KCl. (d) Galvanostatic charge/discharge profiles of CAP-2 at different current densities in 2 M KCl.

modes of isolated lattice, additional space group modes can appear in the spectrum of a semicrystalline polymer due to conformation ordering of the chains, interchain interactions and the symmetry of the crystal subcell, which explains the appearance of well resolved sharp peaks for CAP-2 in Figure 2h.

In 3-TBQP crystals, monomer units are prepacked into a layered structure though a displaced face-to-face $\pi-\pi$ interaction (Figure 1d). In a tightly packed state, cross-coupling directions are affected by steric factors during solid-state polymerization. The orientations of the dangling bonds at C9 and C16 positions after debromination (Figure 4b) determine the morphology of final product. In each layer, 3-TBQP monomers are arranged in a parallel but slightly slipped fashion. Taking monomer B and monomer C in Figure 4d as an example, the angle between C9−Br1 and C16−Br2 is around 109°, thus it requires significant rotation and movements of the monomers to allow C9−C16 coupling. This is not favored due to considerable sterical hindrance in the tightly packed state during solid-state polymerization. On the other hand, C16−C16 coupling between B and C, or between B and D, is favored by the parallelly aligned C16−Br2 bonds. C16−C16 coupling would lead naturally to the formation of CAP-2 (Figure 4e). Thus, it is expected that most of the initial C−C coupling would occur between C16 sites, favoring the formation of a 2-D polymer. The XRD spectrum of CAP-2 shows a peak at ~5.6° (200), which matches well with the theoretical XRD profile produced from DFT optimized bulk CAP-2 structure. However, the (1−10) peak at 7.4° is missing and the (002) peak at ~26.5° is broadened, indicating poor crystallinity for CAP-2. N_2 gas sorption measurement of CAP-2 shows a typical type I isotherm profile for microabsorbents, and an H4 type hysteresis loop, due probably to the irregular pore shape of defects. Its Brunauer−Emmett−Teller (BET) surface area and pore volume derived are SA_{BET} = 594 m^2 g^{-1} and 0.38 cm^3 g^{-1}, respectively. Further, CAP-2 shows a dominant pore size at

around 0.8 nm, close to the theoretical value of DFT optimized bulk CAP-2 structure (7.0 Å). All these data reveal that CAP-2 is a nanocrystalline 2-D porous polymer.

We conducted electrical measurements for both CAP-1 (3-D) and CAP-2 (2-D). As shown in Figure S7a, the electrical conductivities of the intrinsic conjugated polymers are 2.8×10^{-5} S cm^{-1} for CAP-1 and 6.0×10^{-5} S cm^{-1} for CAP-2, which are typical of nondoped conjugated polymers.[18] Overall, the conductivity of CAPs is 1 order of magnitude higher than conjugated porous polymer prepared by solution method with catalysts.[17] It is reasonable that CAP-2, which has a 2-D morphology and a conjugated structure, exhibits a lower resistance than 3-D cross-linked CAP-1. The electrical conductivity of CAPs is further improved once it is cycled in electrolyte due to doping.[19] The electrochemical characteristics of CAPs were first evaluated using a three-electrode cell system in 2 M KCl aqueous electrolyte medium. Figures 5a and 5c show the CV curves of CAP-1 and CAP-2 at different sweep rates from 10 to 100 mV s^{-1} in the potential range from 0 to 1 V, respectively. Compared with CAP-1, CAP-2 shows a higher current density. The CV curves show rectangular-like shapes, indicating good capacitive behavior of the electrode materials where the charges are mainly stored as electric double layer (EDL). In general, conducting polymers with redox properties exhibit pseudocapacitive behavior;[20,21] however, in the present study the EDL capacitive storage is dominant due to the lack of redox functional groups in CAP. It is noted that the current density increases with scan rate and the shape of the CV curves is well maintained, suggesting facile kinetics and good rate capability. We further investigated the electrochemical behavior of CAP-2 in various electrolytes, including 2 M LiCl, 2 M NaCl, 1 M MgCl$_2$ aqueous solution, and ionic liquid electrolyte 1-Ethyl-3-methylimidazolium tetrafluoroborate (EMImBF$_4$) in acetonitrile (1:1 in volume ratio). As shown in Figure S8a, in aqueous LiCl and NaCl electrolyte, CAP-2 have similar behavior to that in aqueous KCl solution. However, CAP-2
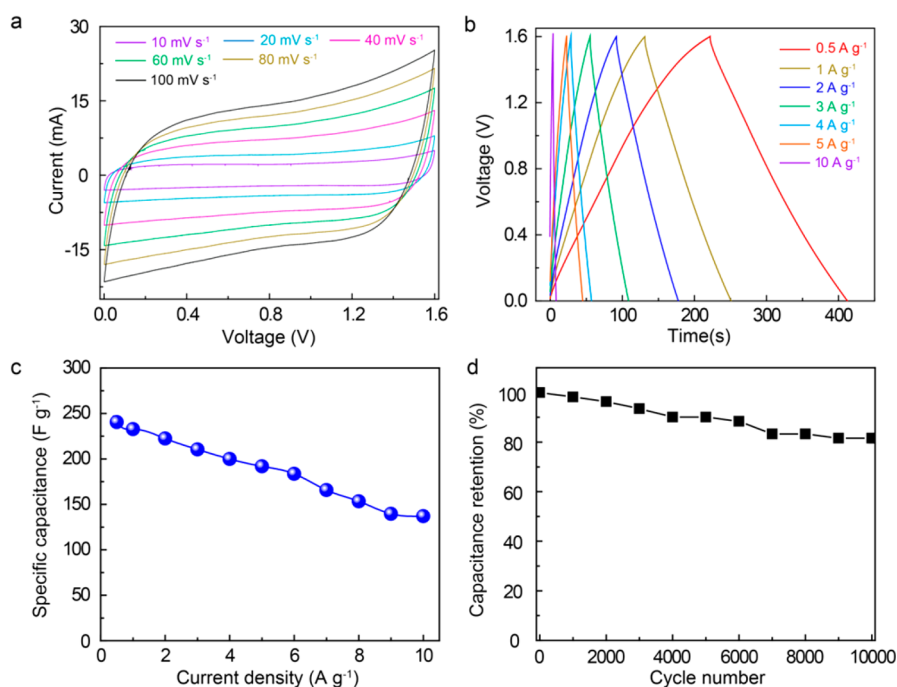
Figure 6. Electrochemical performance of CAP-2 in an asymmetry supercapacitor cell in 2 M KCl. (a) Cyclic voltamograms of the CAP-2 at different scan rates in the potential window of 0−1.6 V. (b) Galvanostatic charge/discharge profiles at various current densities. (c) corresponding specific capacitances of the asymmetric cell. (d) Capacitance retention at first 10 000 cycles at 2 A g^{-1}.

shows much smaller current density in $MgCl_2$ electrolyte, which can be attributed to the slow kinetics of hydrated Mg^{2+} ions.[22,23] In ionic liquid electrolyte $EMImBF_4$ in actonitrile (Figure S8b), CPA-2 shows no obvious capacitive behavior, which may be due to that the pore size is not suitable for the solvated cations of ionic liquid electrolyte.[24]

The galvanostatic charge/discharge curves of CAP-2 sample in 2 M KCl at various current densities are shown in Figure 5d. The potential drop during the discharge process, which is generally caused by the internal resistance of the device, is quite low at only 0.03 V at a discharge current density of 1 A g^{-1}. This suggests good electrical conductivity of CAP-2 and also good interfacial contact between the active material and the current collecting substrate, which contributes to the low overpotential during the charge/discharge process. Table S3 summarizes specific capacitances of CAP-s at various galvanostatic charge/discharge current densities in the three-electrode setup. Even though CAP-1 has a slightly larger specific surface area than CAP-2 (704 vs 594 m^2 g^{-1}), CAP-1 shows only a specific capacity of 81 F g^{-1} at 1 A g^{-1}, which is much lower than that of CAP-2 (240 F g^{-1} at 1 A g^{-1}). The much higher capacitance of CAP-2 is attributed to its layered nanoporous structure. Compared with amorphous CAP-1 where ions transport in a randomly connected 3-D networks is highly impeded, ion transportation through 2-D planes and 1-D channels in the layered CAP-2 is much smoother.[25,26] In addition, a higher N content in CAP-2 is also helpful in improving surface wettability for electrolyte ion transport by modifying the electron donor/acceptor characteristics.[27−29] It is noted that the capacitance of the CAPs decrease gradually with increasing current densities, which might be rate-limited by the adsorption of ions into the active materials.

A more rigorous test of the electrochemical performance was carried out in asymmetric supercapacitors. In the present study, activated carbon (Ac, Kuraray, Japan) and as-prepared CAP-2

were used as negative and positive electrodes, respectively in the asymmetric supercapacitor fabrication. The calculated gravimetric specific capacitance of CAP-2 and AC electrodes from the galvanostatic charge/discharge (GCD) (three electrode system) at 1 A g^{-1} is 240 and 80 F g^{-1}, respectively. In the present case, the mass loading of positive and negative electrode is used in the ratio of 1:3 of (CAP-2, 1.0 mg cm^{-2}: AC, 3.0 mg cm^{-2}), respectively, and 2 M KCl aqueous solution is employed as electrolyte medium throughout the study. As shown in Figure S9, the cell was first cycled at different potential ranges at 20 mV s^{-1}. Obviously, Faradaic electrochemical reactions are promoted when the operating voltage window is increased. However, oxygen evolution occurs when the operating potential reaches 1.8 V. Thus, 1.6 V is employed as the cutoff potential to investigate the electrochemical performance of the asymmetric supercapacitor. The asymmetric supercapacitor was investigated at different scan rates in the potential window of 0 to 1.6 V, as shown in Figure 6a. Similar to that in the three-electrode cell, the current density increases with increasing scan rate and the cell showed good performance even at high scan rate (100 mV s^{-1}), suggesting a good rate capability for energy storage.

The GCD curves of the asymmetric supercapacitor obtained at different current densities are shown in Figure 6b. Charge−discharge curves show a symmetric behavior which implies that the electrochemical reaction is highly reversible, even at a very high currently density of 10 A g^{-1}. The calculated specific capacitances of the cell at different current densities based on the total mass of the two electrodes are summarized in Figure 6c. The specific capacitance of the cell is 233 F g^{-1} at a current density of 1.0 A g^{-1}. The cell shows superior rate capability and retains a high capacitance of 137 F g^{-1} at a very high current density of 10.0 A g^{-1}. To compare the performance of CAP-2 with reported N-doped carbonaceous materials, the normalized capacitances, used electrolytes and major charactericteristics of
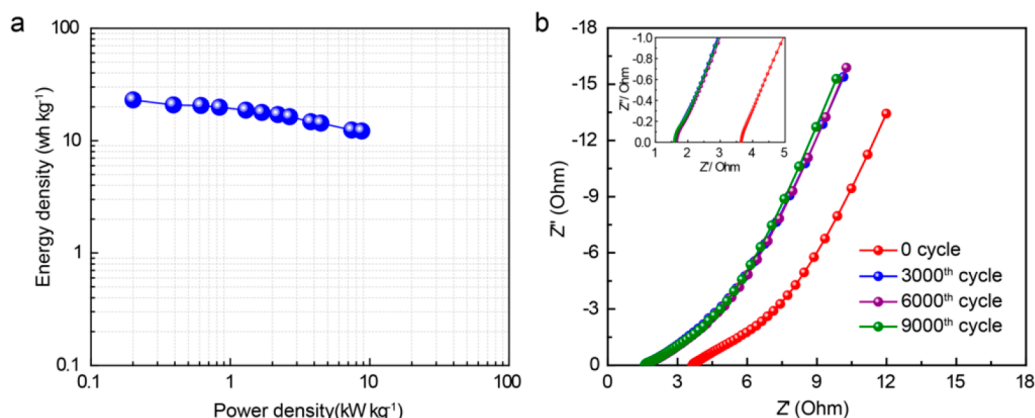
Figure 7. (a) Ragone plot of the asymmetric cell. (b) EIS spectra of CAP-2 at every 3000 cycles in the asymmetric cell (Insert: magnified 1−5 Ω region).

the materials are listed in Table S4. Obviously, the capacitance value of CAP-2 is higher than most of N-enriched carbon materials. The high specific capacitances of CAP-2 are attributed to synergistic effects of a large specific surface area, layered nanoporous structure as well as a high N-doping level, which improves the surface wettability for electrolyte ion transport.[29]

To fully characterize the capacitive performance of CAP-2, the energy densities and power densities of the asymmetric cell are also calculated based on the charging/discharging profiles. Figure 7a shows the Ragone plots of the asymmetric supercapacitor measured in the voltage window of 0 to 1.6 V. The asymmetric capacitor shows a promising energy density of 23 Wh kg^{-1} at a current density of 1A g^{-1}. The cell exhibits a power density of 8.7 kW kg^{-1} at a current density of 10 A g^{-1}, which is much higher than most commercial aqueous-based capacitors.[30,31] The cycle life of the asymmetric cell was further investigated at 2 A g^{-1} (Figure 6d). In general, conducting polymers showed poor cycle stability due to the swelling and shrinkage of the polymer during the charge and discharge process of the cell.[32] However, in the present work, the asymmetric cell shows an excellent cycle life with the capacitance retention of ∼80% over 10, 000 cycles. The layered structure and nanoporous morphology of CAP-2 reduce ion diffusion resistance and enable rapid ion diffusion into the nanopores on the surface of the polymeric layers. Figure 7b shows the EIS spectra of CAP-2 electrode before and after cycling. At the initial stage, the resistance of CAP-2 is comparable to that of the AC electrode (Figure S10). During cycling, the resistance shows negligible impedance changes. It implies that CAP-2 bassed electrode materials have excellent structural stability and remain good electrical contact throughout the cycles.[33,34]

CONCLUSIONS

A 2-D conjugated polymer based on C−C coupling reaction is successfully prepared *via* a facile solid-state polymerization of monomers prepacked in layered crystalline structure. The topological design principle is based on the spatial positioning of radical sites to allow easy cross-coupling and to minimize rotations after debromination using steric effects, thereby achieving controlled 2-D polymerization, as exemplified by CAP-2. The nanoporous morphology and layered structure of CAP-2 enables rapid ion diffusion into its nanopores, thus CAP-2 shows high capacity (233 F g^{-1} at 1 A) and long cycle

life in supercapacitors. Due to its low cost and easy processability, the endogenous polymerization method proposed here should allow 2-D polymer to be scaled up readily for energy storage applications.

EXPERIMENTAL METHODS

Synthesis of 2,7,11,16-Tetrabromotetrabenzo[a,c,h,j]-phenazine (2-TBTBP). 2,7-Dibromophenanthrene-9,10-diaminium chloride (2,7-DBPDA) was synthesized from 2,7-dibromophenan-threne-9,10-dione (2,7-DBPD, purchased from Tokyo Chemical Industry) according to the literature.[35] To prepare 2-TBTBP, 2,7-DBPD (1.0 mmol, 0.366 g) and 2,7-DBPDA (1.0 mmol, 0.439 g) were transferred into a round button flask with a magnetic spin bar, and suspended in 50 mL acetic acid to make a suspension in Ar atmosphere, and heated to 100 °C. After the addition of 1.0 mL triethylamine, the mixture immediately changed to yellow color, and was further refluxed at 130 °C for 6 h. Once cooled to room temperature, the mixture was diluted with acetic acid and poured into 200 mL of water. The yellow precipitate was collected and exhaustively washed by Soxhlet extraction with water, ethanol, chloroform, THF, N,N-dimethylformamide and ethanol again, and dried at 120 °C overnight in vacuum oven to yield 2,7,11,16-tetrabromotetrabenzo-[a,c,h,j]phenazine (2-TBTBP) as yellow-colored powder (0.65g, 94%). Elemental analysis (%): calculated for (C$_{28}$H$_{12}$Br$_4$N$_2$): C, 48.32; H, 1.74; N, 4.02; Br, 45.92; found: C, 47.62, H, 2.01, N, 4.04, Br 45.75. MALDI-TOF mass (negative mode) m/z = 697.5 (calcd. 696.0); No solution NMR data was collected due to its poor solubility. Its structure was confirmed with single crystal X-ray diffraction analysis. CCDC 1561712 contains the supplementary crystallographic data for this compound. These data can be obtained free of charge from The Cambridge Crystallographic Data Centre *via* www.ccdc.cam.ac.uk/data_request/cif.

Synthesis of 3,6,14,17-Tetrabromodibenzo[a,c]dibenzo-[5,6:7,8]quinoxalino-[2,3-i]phenazine (3-TBQP). 3,6-Dibromo-phenanthrene-9,10-dione (3,6-DBPD purchased from Shanghai Yu Rui Chemical Co., Ltd., 0.76 g, 2.1 mmol), and benzene-1,2,4,5-tetraamine tetrahydrochloride (0.28 g, 1.0 mmol) were transferred into a round button flask with a magnetic spin bar, and suspended in 6 mL of ethanol and 20 mL of acetic acid to make a brown suspension in Ar atmosphere, and heated to 100 °C. After the addition of 1.0 mL of triethylamine, the mixture immediately changed to red color, and was further refluxed at 130 °C for 6 h. Once cooled to room temperature, the mixture was diluted with acetic acid and poured into 200 mL of water. The red precipitate was collected and exhaustively washed by Soxhlet extraction with water, ethanol, chloroform, THF, N,N-dimethylformamide and ethanol again, and dried at 120 °C overnight in vacuum oven to yield 3-TBQP as copper-colored powder (0.78 g, yield 97%). Elemental analysis (%): calculated for (C$_{34}$H$_{14}$Br$_4$N$_4$): C, 51.16, H, 1.77, N, 7.02, Br, 40.05; found: C, 50.87, H, 2.01, N, 7.06, Br 39.76. MALDI-TOF mass (negative mode) m/z = 799.8 (calcd.

798.1); No solution NMR data was collected due to its poor solubility. Its structure was confirmed with single crystal X-ray diffraction analysis. CCDC 1561713 contains the supplementary crystallographic data for this compound. These data can be obtained free of charge from The Cambridge Crystallographic Data Centre *via* www.ccdc.cam.ac.uk/data_request/cif.

Single Crystals Growth. Crystals were grown in a three-zone electric furnace with a stream of Ar gas flow. Typically, 200 mg of as-prepared crude compound was placed on a quartz boat and inserted into a 25 mm quartz tube. The tube was placed in the furnace and connected to a supply of Ar. The Ar flow was adjusted to 50 mL min^{-1} under vacuum ($\sim$30 Pa). The first zone containing the initial sample and was heated to 350 °C for 2-TBTBP, and 380 °C for 3-TBQP to promote volatilization. The second zone was the region of molecular transport and was heated to 320 °C. The temperature of the third zone was maintained at 260 °C to allow crystal deposition. These conditions yielded needle-shaped crystals $\sim$200 μm in width and over 1 mm in length, which were deposited on the quartz tube wall in about 2 h for 2-TBTBP, and 24 h for 3-TBQP, respectively. About 60% yield can be obtained based on the amount sublimed and the single crystal products collected.

Crystallography Data Collection. The X-ray data were collected with a Bruker AXS D8 Venture Kappa four cycles X-ray diffractometer system equipped with a Photon 100 detector, using a Mo sealed microfocusing Source, with the Bruker Apex 2 suite program. Data were integrated with the Bruker SAINT program using a narrow-frame algorithm. SADABS was used for absorption correction. Structural solution and refinement were carried out with the SHELXTL suite of programs. The structures were solved by direct methods, followed by difference maps and refined with full-matrix least-squares on F2. All non-hydrogen atoms were generally given anisotropic displacement parameters in the final model. All hydrogen atoms were put at calculated positions.

Thermal Initiated Solid-State Polymerization. Typically, a quartz tube holding precursor crystals (200 mg) was paced in a tube furnace under an Ar flow of 100 mL min^{-1} (Figure S2). The quartz tube was heated at 10 °C min^{-1} to 520 °C and maintained at 520 °C for 3 h to complete the polymerization. Finally, the tube furnace was cooled down to room temperature at 2 °C min^{-1}. The yield for CAP-1 and CAP-2 are 95% and 99%, respectively.

Structure Characterization. Scanning electronic microscopy (SEM) images were collected with Jeol JSM-6701F. The bulk polymers were mechanically exfoliated onto clean Si/SiO$_2$ substrates using scotch-tape method. Prior to exfoliation, the Si/SiO$_2$ substrates were subjected to mild O$_2$ plasma treatment to remove organic contaminants. Atomic force microscopy (AFM) was then used to determine the thickness of the exfoliated flakes. AFM were performed using a Bruker Dimension FastScan Atomic Force Microscope in tapping mode at room temperature. Samples were crushed into fine powder and dispersed on gold-covered Si wafer for X-ray photoelectron spectroscopy (XPS) investigations, which were performed with the Phobios 100 electron analyzer equipped with 5 channeltrons, using an unmonochromated Al Ka X-ray source (1486.6 eV). Fourier-transform infrared spectroscopy (FTIR) measurements were performed at RT in a continuous vacuum environment. The FTIR samples were prepared by compressing samples with KBr into a disc. UV−vis−NIR (Shimadzu UV-3600), solid ^{13}C NMR spectra were recorded with Bruker 400 MHz. Gas sorption measurements were performed with samples polymerized from precursor powders without further sublimation, on a Micromeritics ASAP 2020 with micropore option. N2 analyses were performed at 77 K using a liquid N$_2$ bath. Thermal gravimetric analysis (TGA) of the single crystals was performed in the range of 150 to 900 °C at a heating rate of 10 °C min^{-1} in nitrogen atmosphere.

Electrochemical Characterization. The working electrode slurry was prepared by mixing CAPs or activated carbon (AC), Super p carbon black (conductive additive) and poly(vinyldifluoride) (PVDF) (binder) at a weight ratio of 80:15:05 thoroughly in *N*-methylpyrrolidone (NMP) solvent. The obtained homogeneous slurry was coated on graphite paper and then dried in vacuum oven at 80 °C overnight to obtain the working electrodes. Cyclic voltammetry (CV), galvanostatic charge−discharge (GCD), and electrochemical impedance spectroscopy (EIS), were recorded using an electrochemical workstation (Solartron, 1470E).

A laboratory-type three electrode set up was used for testing the specific properties of the samples at first. The CAP based electrode with a loading of 1.0 mg cm^{-2} was used as working electrode. A Pt strip and SCE were employed as counter electrode and reference electrode, respectively. The gravimetric specific capacitances for the three-electrode cell were calculated from the galvanostatic charge−discharge curves using the following equation:

$$C = I \times \Delta t / mV$$

where I (A) is the current, t (s) is the discharge time, m (g) is the mass of the working electrode, and V (V) is the discharge potential range.

For the asymmetric supercapacitor, two electrodes cell setup was constructed using CAP-2 and AC as positive electrode and negative electrode, respectively. The optimized active materials loading ratio 1:3 was obtained from the three electrode cell result. The mass loadings of active materials are about 1.0 (CAP-2) and 3.0 mg cm^{-2} (AC, Kuraray, Japan) respectively. The cell voltage was optimized and the maximum cell voltage is about 1.6 V at safe condition. The gravimetric specific capacitance of the asymmetric cell is calculated as

$$C_{\text{spec}} = 4(I \times \Delta t / m \times \Delta V)$$

where I (A) is the current, t (s) is the discharge time, m (g) is the total mass of the two electrodes, and V (V) is the discharge potential range.

The energy density is obtained as

$$E = CV_{\text{M}}^2 / 8$$

where C is the gravimetric specific capacitance and V_{M} is the maximum testing potential (1.6 V).

The power density is calculated as

$$P = E / \Delta t$$

where E is energy density and Δt is the discharge time.

ASSOCIATED CONTENT

Ⓢ Supporting Information

The Supporting Information is available free of charge on the ACS Publications website at DOI: 10.1021/acsnano.7b08354.

> Thermal gravimetric analysis of precursors, XPS spectra and FTIR spectra of precursors and CAPs, additional AFM images of CAP-2, elemental analysis results, Nyquist plots of CAPs, additional electrochemical measurements of CAP-2 electrodes, crystallographic data of precursors and atomic coordinates of DFT optimized CAP-2 units cell (PDF)
> Crystal data (CIF)
> Crystal data (CIF)

AUTHOR INFORMATION

Corresponding Author
*E-mail: chmlohkp@nus.edu.sg.

ORCID ⊙
Wei Liu: 0000-0002-6812-6107
Mani Ulaganathan: 0000-0003-4085-0133
Ibrahim Abdelwahab: 0000-0002-0107-5827
Sherman Jun Rong Tan: 0000-0003-1591-3497
Yang Bao: 0000-0001-9868-4946
Jianyi Chen: 0000-0002-3757-7634
Kian Ping Loh: 0000-0002-1491-743X

Present Addresses

[⊥]CSIR—Central Electrochemical Research Institute (CECRI), Karaikudi, Tamil Nadu, 630003, India.

[¶]Department of Applied Physics, Hong Kong Polytechnic University, Hong Kong.

Author Contributions

[#]W.L. and M.U. contributed equally.

Notes

The authors declare no competing financial interest.

REFERENCES

(1) Miller, J. R.; Simon, P. Materials Science: Electrochemical Capacitors for Energy Management. *Science* **2008**, *321*, 651−652.

(2) Burke, A. R&D Considerations for the Performance and Application of Electrochemical Capacitors. *Electrochim. Acta* **2007**, *53*, 1083−1091.

(3) Zhang, L. L.; Zhao, X. S. Carbon-Based Materials as Supercapacitor Electrodes. *Chem. Soc. Rev.* **2009**, *38*, 2520−2531.

(4) Cooper, A. I. Conjugated Microporous Polymers. *Adv. Mater.* **2009**, *21*, 1291−1295.

(5) Vilela, F.; Zhang, K.; Antonietti, M. Conjugated Porous Polymers for Energy Applications. *Energy Environ. Sci.* **2012**, *5*, 7819−7832.

(6) Xu, Y.; Jin, S.; Xu, H.; Nagai, A.; Jiang, D. Conjugated Microporous Polymers: Design, Synthesis and Application. *Chem. Soc. Rev.* **2013**, *42*, 8012−8031.

(7) Waller, P. J.; Gándara, F.; Yaghi, O. M. Chemistry of Covalent Organic Frameworks. *Acc. Chem. Res.* **2015**, *48*, 3053−3063.

(8) DeBlase, C. R.; Silberstein, K. E.; Thanh-Tam, T.; Abruna, H. D.; Dichtel, W. R. β-Ketoenamine-Linked Covalent Organic Frameworks Capable of Pseudocapacitive Energy Storage. *J. Am. Chem. Soc.* **2013**, *135*, 16821−16824.

(9) Feng, X.; Ding, X.; Jiang, D. Covalent Organic Frameworks. *Chem. Soc. Rev.* **2012**, *41*, 6010−6022.

(10) Kissel, P.; Murray, D. J.; Wulftange, W. J.; Catalano, V. J.; King, B. T. A Nanoporous Two-Dimensional Polymer by Single-Crystal-to-Single-Crystal Photopolymerization. *Nat. Chem.* **2014**, *6*, 774−778.

(11) Kory, M. J.; Wörle, M.; Weber, T.; Payamyar, P.; van de Poll, S. W.; Dshemuchadse, J.; Trapp, N.; Schlüter, A. D. Gram-Scale Synthesis of Two-Dimensional Polymer Crystals and their Structure Analysis by X-ray Diffraction. *Nat. Chem.* **2014**, *6*, 779−784.

(12) Kissel, P.; Erni, R.; Schweizer, W. B.; Rossell, M. D.; King, B. T.; Bauer, T.; Götzinger, S.; Schlüter, A. D.; Sakamoto, J. A Two-Dimensional Polymer Prepared by Organic Synthesis. *Nat. Chem.* **2012**, *4*, 287−291.

(13) Liu, W.; Loh, K. P. Two-Dimensional Conjugated Polymers Based on C−C Coupling. *Acc. Chem. Res.* **2017**, *50*, 522−526.

(14) Ben, T.; Ren, H.; Ma, S.; Cao, D.; Lan, J.; Jing, X.; Wang, W.; Xu, J.; Deng, F.; Simmons, J. M.; Qiu, S.; Zhu, G. Targeted Synthesis of a Porous Aromatic Framework with High Stability and Exceptionally High Surface Area. *Angew. Chem., Int. Ed.* **2009**, *48*, 9457−9460.

(15) Yuan, D.; Lu, W.; Zhao, D.; Zhou, H. Highly Stable Porous Polymer Networks with Exceptionally High Gas-Uptake Capacities. *Adv. Mater.* **2011**, *23*, 3723−3725.

(16) Liu, W.; Luo, X.; Bao, Y.; Liu, Y. P.; Ning, G.; Abdelwahab, I.; Li, L.j.; Nai, C. T.; Hu, Z. G.; Zhao, D.; Hu, Z. G.; Zhao, D.; Liu, B.; Quek, S. Y.; Loh, K. P. A Two-Dimensional Conjugated Aromatic Polymer *via* C−C Coupling Reaction. *Nat. Chem.* **2017**, *9*, 563−570.

(17) Sakaushi, K.; Hosono, E.; Nickerl, G.; Gemming, T.; Zhou, H.; Kaskel, S.; Eckert, J. Aromatic Porous-Honeycomb Electrodes for a Sodium-Organic Energy Storage Device. *Nat. Commun.* **2013**, *4*, 1485−1491.

(18) MacDiarmid, A. G. Synthetic Metals": A Novel Role for Organic Polymers (Nobel Lecture). *Angew. Chem., Int. Ed.* **2001**, *40*, 2581−2590.

(19) Pei, Q. B.; Yu, G.; Zhang, C.; Yang, Y.; Heeger, A. J. Polymer Light-Emitting Electrochemical Cells. *Science* **1995**, *269*, 1086−1088.

(20) Zhang, K.; Zhang, L. L.; Zhao, X. S.; Wu, J. S. Graphene/Polyaniline Nanofiber Composites as Supercapacitor Electrodes. *Chem. Mater.* **2010**, *22*, 1392−1401.

(21) Filippo, M.; Jian, Y.; Wesley, W.; Fred, W. A Low Band Gap Conjugated Polymer for Supercapacitor Devices. *J. Phys. Chem. B* **2006**, *110*, 22202−22206.

(22) Rodriguez-Cruz, S. E.; Jockusch, R. A.; Williams, E. R. Hydration Energies and Structures of Alkaline Earth Metal Ions, $M_2^+(H_2O)_n$, n = 5−7, M = Mg, Ca, Sr, and Ba. *J. Am. Chem. Soc.* **1999**, *121*, 8898.

(23) Lightstone, F. C.; Schwegler, E.; Hood, R. Q.; Gygi, F.; Galli, G. A first Principles Molecular Dynamics Simulation of the Hydrated Magnesium Ion. *Chem. Phys. Lett.* **2001**, *343*, 549−555.

(24) Sillars, F. B.; Fletcher, S. I.; Mirzaeian, M.; Hall, P. J. Effect of Activated Carbon Xerogel Pore Size on the Capacitance Performance of Ionic Liquid Electrolytes. *Energy Environ. Sci.* **2011**, *4*, 695−706.

(25) Liu, C. G.; Yu, Z.; Neff, D.; Zhamu, A.; Jang, B. Z. Graphene-Based Supercapacitor with an Ultrahigh Energy Density. *Nano Lett.* **2010**, *10*, 4863−4868.

(26) Choi, B. G.; Yang, M.; Jung, S. C.; Lee, K. G.; Kim, J.-G.; Park, H.; Park, T. J.; Lee, S. B.; Han, Y.-K.; Huh, Y. S. Enhanced Pseudocapacitance of Ionic Liquid/Cobalt Hydroxide Nanohybrids. *ACS Nano* **2013**, *7*, 2453−2460.

(27) Jeong, H. M.; Lee, J. W.; Shin, W. H.; Choi, Y. J.; Shin, H. J.; Kang, J. K.; Choi, J. W. Nitrogen-Doped Graphene for High-Performance Ultracapacitors and the Importance of Nitrogen-Doped Sites at Basal Planes. *Nano Lett.* **2011**, *11*, 2472−2477.

(28) Wen, Z.; Wang, X.; Mao, S.; Bo, Z.; Kim, H.; Cui, S.; Lu, G.; Feng, X.; Chen, J. Crumpled Nitrogen-Doped Graphene Nanosheets with Ultrahigh Pore Volume for High-Performance Supercapacitor. *Adv. Mater.* **2012**, *24*, 5610−5616.

(29) Wang, G.; Zhang, L.; Zhang, J. A Review of Electrode Materials for Electrochemical Supercapacitors. *Chem. Soc. Rev.* **2012**, *41*, 797−828.

(30) Zhu, Y.; Murali, S.; Stoller, M. D.; Ganesh, K. J.; Cai, W.; Ferreira, P. J.; Pirkle, A.; Wallace, R. M.; Cychosz, K. A.; Thommes, M.; Su, D.; Stach, E. A.; Ruoff, R. S. Carbon-Based Supercapacitors Produced by Activation of Graphene. *Science* **2011**, *332*, 1537−1541.

(31) Cao, C.-Y.; Guo, W.; Cui, Z.-M.; Song, W.-G.; Cai, W. Microwave-Assisted Gas/Liquid Interfacial Synthesis of Flower-Like NiO Hollow Nanosphere Precursors and their Application as Supercapacitor Electrodes. *J. Mater. Chem.* **2011**, *21*, 3204−3209.

(32) Snook, G. A.; Kao, P.; Best, A. S. Conducting-Polymer-Based Supercapacitor Devices and Electrodes. *J. Power Sources* **2011**, *196*, 1−12.

(33) Yang, L.; Cheng, S.; Ding, Y.; Zhu, X.; Wang, Z. L.; Liu, M. Hierarchical Network Architectures of Carbon Fiber Paper Supported Cobalt Oxide Nanonet for High-Capacity Pseudocapacitors. *Nano Lett.* **2012**, *12*, 321−325.

(34) Chen, Q. L.; Xue, K. H.; Shen, W.; Tao, F. F.; Yin, S. Y.; Xu, W. Fabrication and Electrochemical Properties of Carbon Nanotube Array Electrode for Supercapacitors. *Electrochim. Electrochim. Acta* **2004**, *49*, 4157−4161.

(35) Martin, P.; Nikola, K.; Albrecht, M. Diastereoselective Reaction of (MP)-Pentahelicene-7,8-Dione with Trans-Cyclohexane-1,2-Diamine. Thermal and Photochemical Transformations of its Product. *Tetrahedron: Asymmetry* **2002**, *12*, 3333−3342.